10 Active lidar remote sensing

M. Patrick McCormick and Kevin R. Leavor

10.1 Introduction

Lidar, an acronym for "**LI**ght **D**etection **A**nd **R**anging", is an active remote sensing technique analogous to radar. Lidar systems use a laser as an active radiation source. The short pulse lengths produced by a laser (approximately 20 ns) and the spectral bandwidth (1 cm^{-1}) allow for highly-resolved ranging measurements with high signal-to-noise. Also, as in radar, lidars could be either monostatic (collocated transmitter and receiver) or bistatic (separated transmitter and receiver). Figure 10.1 illustrates an operational, monostatic lidar. Laser radiation is transmitted and scattered or absorbed by atmospheric constituents, such as clouds, aerosols, or molecules. Photons scattered back to the receiver are then collected, directed to a detector whose signal is analog-to-digitally recorded or counted as a function of altitude or range. The strength of the return signal is related to the physical and optical properties of the scatterers.

Lidar is an active remote sensing instrument with the laser providing the radiation source, and is able to take measurements in the absence of a natural source of radiation. Comparatively, passive remote sensing instruments such as those using the occultation technique, for example, require a natural radiation source such as the sun or stars. Lidar's requirement is that the laser signal is strong enough to overcome any background noise. Active remote sensing instruments typically do not have an ability to self-calibrate, unlike some passive sensors like those that measure unattenuated, exo-atmospheric radiation, just before or after the atmospheric measurements, or those that carry on-board blackbody sources as a means of calibration.

Lidar is one of the only techniques and, if considering only remote sensing techniques, is probably the only technique that can provide routine, height-resolved observations of aerosols and their characteristics in the low-to-middle atmosphere. Lidar measurements from ground-based, aircraft and spacecraft systems are now commonplace. Whereas the

J. Lenoble et al. (eds.), *Aerosol Remote Sensing*, Springer Praxis Books,
DOI 10.1007/978-3-642-17725-5_10,

ground-based systems are capable of producing long-term observations from a fixed or local location, aircraft up-looking and down-looking lidars can produce data sets over regional areas and spacecraft can produce years of observations on a near global basis, depending on spacecraft orbital characteristics. Networks of ground-based lidar systems, ranging from generalized systems found in the European EARLINET and worldwide GALION networks, to arrays of specialized systems such as Goddard Space Flight Center's MPLNET consisting of micropulse lidars, provide the capability to study primarily regional characterization of aerosols and their dynamical effects with time and space.

Elastic backscatter lidars were developed soon after the successful optical pumping of ruby material in the Hughes Corporation laboratory, producing stimulated optical emission at 694.3 nm (Maiman, 1960), and the invention of a technique for producing a giant pulse by Q-switching ruby in 1962 (McClung and Hellarth, 1962). The first, atmospheric aerosol lidar measurements were reported by Fiocco and Grams (1964) showing stratospheric aerosol profiling.

The equation governing the strength of the lidar return signal is known as the Lidar Equation, and is given by:

$$P(R) = P_0 \eta \left(\frac{A}{R^2} \right) \left(\frac{c\Delta t}{2} \right) O(R) \sigma_b(R) \exp\left[-2 \int_0^R \sigma_e(r) \mathrm{d}r \right]. \tag{10.1}$$

$P(R)$ is the power of the return signal from range R[1], P_0 is the emitted laser power, η[2] is the system efficiency, A is the receiver's effective area, c is the speed of light, and Δt is the laser's pulse duration. $O(R)$ is an overlap factor that accounts for the separation of the transmitter and receiver optical axes, the transmitter's output size, shape, and divergence and the receiver's field-of-view and imaging properties. The latter determines whether the entirety of the laser backscatter can be imaged on the detector. $\sigma_b(R)$ is the backscatter coefficient of the atmosphere at range R, and $\sigma_e(r)$ is the atmospheric extinction coefficient at range r.

The expression

$$A\left[\frac{c\Delta t}{2} \right] \left[\frac{O(R)}{R^2} \right]$$

represents the factors related to lidar viewing geometry. Figure 10.2 illustrates the presentation of these terms for a typical lidar geometry. Under ideal conditions, the overlap between the laser's output divergence and receiver's field of view equals unity for concentric laser and receivers. In the event that the laser's return is only partially captured by the receiver, $O(R) < 1$. For a given pulse, the effective pulse length is equal to $c\Delta t/2$. Finally, the solid angle into which photons are scattered is A/R^2.

1 Note, throughout Chapter 10 the variable 'R' denotes the range of the lidar beam, while in preceding chapters it represented the reflectance coefficient of a Lambert surface.

2 In Chapter 10, the variable η denotes the system efficiency, while in the preceding chapters it represents the fine mode weighting.

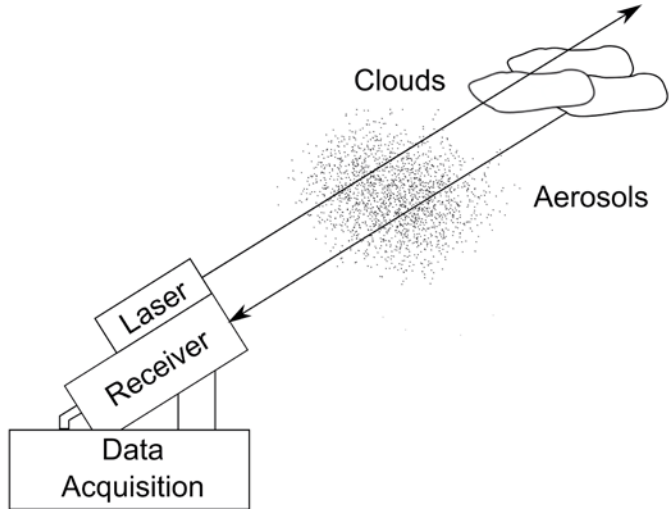

Figure 10.1 An illustration of a monostatic lidar system in operation.

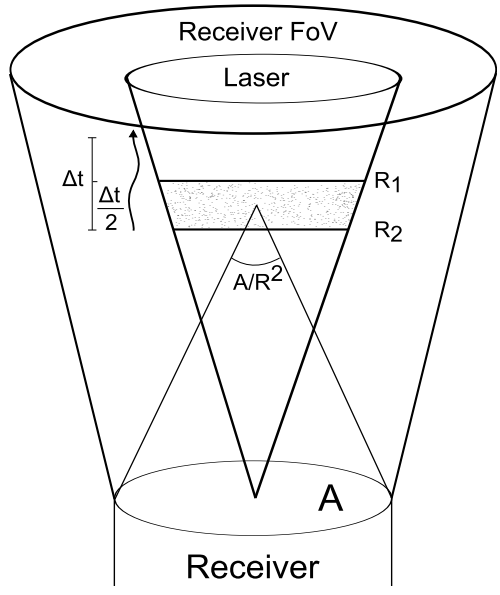

Figure 10.2 Coaxial lidar viewing geometry.

As A and Δt are constant, $O(R)/R^2$ is treated as the geometric factor, denoted

$$G(R) = \frac{O(R)}{R^2}. \tag{10.2}$$

Furthermore, we may define a system constant

$$C = P_0 \eta \left(\frac{c\Delta t}{2} \right) A. \tag{10.3}$$

Equation (10.3) is referred to as the lidar constant. This term describes a lidar's operational capabilities, containing the laser's output, the qualities of the receiving optics, and any signal losses or gains that are the result of instrumentation, such as blocking or interference filters.

The backscatter coefficient, $\sigma_b(R)$, is a description of the atmosphere's tendency to scatter light in the π direction during photon collisions (or, for bistatic systems, in the direction of the receiver). σ_b is usually given in units of $km^{-1}sr^{-1}$.

Finally, $\sigma_e(r)$, the extinction coefficient, is a measure of the loss of photons as the laser pulse travels through the atmosphere, with units commonly expressed in km^{-1}. The integral of the extinction from an origin to range R,

$$\tau = \int_0^R \sigma_e(r) \mathrm{d}r, \tag{10.4}$$

is referred to as optical depth. This expression is doubled in the lidar equation to account for attenuation to the scattering particles and back to the receiver. Bistatic systems express this as the sum of integrals along the path from the laser to the scatterers, and then from the scatterers to the receiver, with each path having a different extinction. For monostatic lidars, when exponentiated, Eq. (10.4) represents a lidar transmission term,

$$T(R) = \exp\left[-2\int_0^R \sigma_e(r) \mathrm{d}r \right], \tag{10.5}$$

Equation (10.1) may then be expressed in the simplified form (Fernald et al., 1972),

$$P(R) = CG(R)\sigma_b(R)T(R). \tag{10.6}$$

Another useful expression is the range-corrected lidar signal,

$$X(R) = R^2 P(R). \tag{10.7}$$

It should be noted that due to the nature of lidar measurements, used to determine the presence of aerosols, clouds, etc., both $\sigma_b(R)$ and $\sigma_e(R)$ are unknown. As a result, external knowledge is often required, either in the form of models, measurements, or assumptions for one of the quantities.
A final expression,

$$L(R) = \frac{\sigma_e(R)}{\sigma_b(R)}, \tag{10.8}$$

known as the lidar ratio, or extinction-to-backscatter ratio, may also be determined. Knowledge of $L(R)$ provides a substitution in Eq. (10.1) for either $\sigma_e(R)$ or $\sigma_b(R)$. A significant source for information on lidar and its uses can be found in Weitkamp (2005).

The following sections detail some of the techniques and lidar measurements involved in the solution of Eq. (10.1) for the extinction and backscatter coefficients. The first section discusses the Fernald inversion method of determining the coefficients from single-wavelength lidar measurements. Although it uses information from only one wavelength, the Fernald method requires assumptions to be made concerning the extinction and scattering properties of the region being measured. This is because each elastic lidar measurement involves two unknown quantities that cannot be determined uniquely from measurements at one wavelength without further constraints. Other lidar techniques, which take advantage of distinctive spectral differences in gaseous absorption (DIAL) and scattering from molecular excitation (Raman) and thermal Doppler broadening (HSRL) effects, are discussed in later sections. These methods require fewer assumptions than the Fernald method and can be used in combination to derive more quantitative information on aerosol physical characteristics.

10.2 Aerosols and elastic backscatter

Since its initial use in atmospheric sciences, lidar has been used extensively for detection of aerosols (Fiocco and Smullin, 1963). Lidar measurements exploit σ_e and σ_b as sums of individual scatterers. As a result, σ_e and σ_b may be written as

$$\sigma_e(R) = \sigma_{e,a}(R) + \sigma_{e,m}(R), \tag{10.9}$$

$$\sigma_b(R) = \sigma_{b,a}(R) + \sigma_{b,m}(R). \tag{10.10}$$

The secondary subscripts "a" and "m" represent contributions due to aerosols and molecules, respectively. Typically, absorption due to molecules can be ignored by using laser wavelengths outside wavelengths in gaseous absorption bands. In this case, only contributions due to molecular scattering need be considered.

Elastic backscatter lidar represents the simplest form of lidar measurement. Typically, a single wavelength is used, and photons from the laser are scattered elastically back to the receiver with no energy lost during the collision, assuming no shift in wavelengths or major gaseous absorption events. Equation (10.1) can then be written

$$X(R)=C\left[\sigma_{b,a}(R)+\sigma_{b,m}(R)\right]\exp\left\{-2\int_0^R\left[\sigma_{e,a}+\sigma_{e,m}(r)\right]\mathrm{d}r\right\}\quad , \tag{10.11}$$

assuming complete overlap at the scattering layer so that $O(R) = 1$.

Equation (10.8) can be expressed as a molecular or aerosol ratio. The molecular lidar ratio is

$$L_m(R)=\frac{\sigma_{e,m}(R)}{\sigma_{b,m}(R)}=\frac{8\pi}{3}sr. \tag{10.12}$$

Note that the molecular lidar ratio is not range-dependent, as the molecular composition of the atmosphere is homogeneous throughout regions used for typical lidar retrievals. This is especially true of aerosol retrievals.

The corresponding aerosol lidar ratio is, however, range-dependent, as the number density and composition of aerosols typically change from any one position in the atmosphere to another. The aerosol lidar ratio, L_a is given simply as

$$L_a(R)=\frac{\sigma_{e,a}(R)}{\sigma_{b,a}(R)}. \tag{10.13}$$

To further simplify Eq. (10.11), the quantity

$$Y(R)=L_a(R)\left[\sigma_{b,a}(R)+\sigma_{b,m}(R)\right] \tag{10.14}$$

is also defined (Sasano et al., 1985). Note that Eq. (10.14) utilizes the backscatter coefficient in the definition as opposed to extinction, as measurements from lidar are generally of backscatter (or attenuated backscatter, prior to analysis).

Substituting Equations (10.12) and (10.13) into Eq. (10.11) to replace the extinction coefficient terms $\sigma_{e,a}$ and $\sigma_{e,m}$ yields

$$X(R)=C\left[\sigma_{b,a}(R)+\sigma_{b,m}(R)\right]\exp\left\{-2\int_0^R\left[L_a\sigma_{b,a}+L_m\sigma_{b,m}(r)\right]\mathrm{d}r\right\}.$$

Adding and subtracting the quantity $L_a\sigma_{b,m}$ to the integral in the exponent, multiplying both sides of the equation by $L_a(R)$, substituting Eq. (10.14), and rearranging gives

$$X(R)L_a(R)\exp\left\{-2\int_0^R\left[L_a(r)-L_m\right]\sigma_{b,m}(r)\mathrm{d}r\right\}=CY(R)\exp\left[-2\int_0^R Y(r)\,\mathrm{d}r\right]. \tag{10.15}$$

Differentiating the logarithm of both sides of Eq. (10.15) with respect to R produces the differential equation

$$\frac{\mathrm{d}\ln\left[X(R)L_a(R)\exp\left\{-2\int_0^R\left[L_a(r)-L_m\right]\sigma_{b,m}(r)\mathrm{d}r\right\}\right]}{\mathrm{d}R}=\frac{1}{Y(R)}\frac{\mathrm{d}Y(R)}{\mathrm{d}R}-2Y(R). \tag{10.16}$$

Note that Eq. (10.16) is a Bernoulli differential equation which can be arranged into the standard form of

$$\frac{dy}{dx}+P(x)y=Q(x)y^n. \tag{10.17}$$

Equation (10.16) is solved using the boundary condition at reference range R_0

$$Y(R_0)=L_a(R_0)\left[\sigma_{b,a}(R_0)+\sigma_{b,m}(R_0)\right], \tag{10.18}$$

which yields

$$\sigma_{b,a}(R)+\sigma_{b,m}(R)=\frac{X(R)\exp\left\{-2\int_{R_0}^R\left[L_a(r)-L_m\right]\sigma_{b,m}(r)\mathrm{d}r\right\}}{\frac{X(R_0)}{\sigma_{b,a}(R_0)+\sigma_{b,m}(R_0)}-2\int_{R_0}^R L_a(r)X(r)T(R_0,r)\mathrm{d}r}, \tag{10.19}$$

where

$$T(R_0,r)=\exp\left\{-2\int_{R_0}^r\left[L_a(r')-L_m\right]\sigma_{b,m}(r')dr'\right\}.$$

Equation (10.19) expresses the aerosol ($\sigma_{b,a}$) and molecular ($\sigma_{b,m}$) backscatter coefficients at range R as a function of the range-corrected lidar return (X), the molecular lidar ratio (L_m), and the assumed aerosol lidar ratio (L_a) integrated from the reference range R_0 to the scattering range. The aerosol lidar ratio is normally assumed to be constant along the laser path. The reference range could be taken as an upper (aerosol-free) region, and the integral evaluated back towards the laser.

This treatment is commonly referred to as the "Fernald method" (Fernald, 1984) or "Klett Method" (Klett, 1981). Molecular scattering could be modeled (for known temperature and pressure) or otherwise derived in order to produce backscatter due to aerosols. Aerosol extinction may then be determined from Eq. (10.13). Figure 10.3 shows measurements of aerosol extinction coefficient over Hampton University with respect to time (left) and a time-averaged profile (right) using the above method. Higher values of aerosol extinction are seen within the Planetary Boundary Layer (PBL), below approximately 3 km, with less loading above in the free troposphere. Higher levels of aerosol extinction are measured higher in the atmosphere, most likely due to clouds.

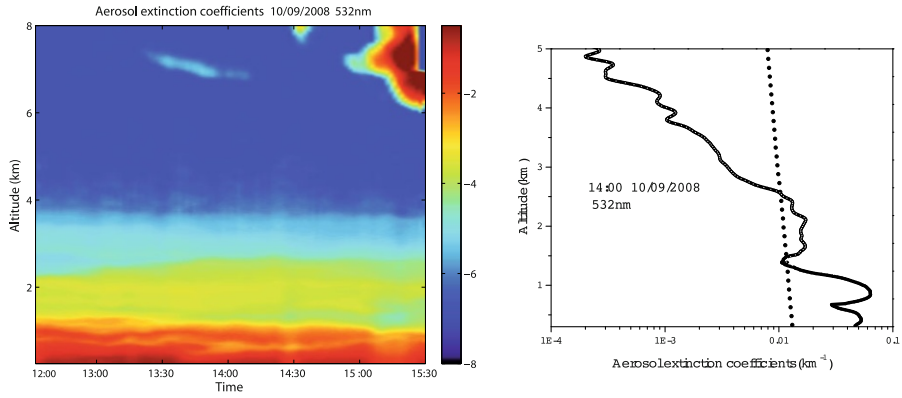

Figure 10.3 Measurements of aerosol extinction coefficient (km^{-1}) over Hampton University on October 9, 2008. Note: The color scale in the left panel is logarithmic such that -3 is equivalent to e^{-3}. The dotted line in the right panel is the corresponding molecular extinction as a function of altitude.

The Fernald method shows that aerosol retrievals are possible with a single wavelength lidar, but assumptions have to be made. For example, one must assume a lidar ratio, typically using a priori knowledge of the types of aerosols to be measured. Furthermore, aerosol retrievals are typically normalized to an aerosol-free region of the atmosphere (e.g., the middle stratosphere or free troposphere). However, in cases of high aerosol loading, such as during fires or volcanic eruptions, a particular lidar system either might not have the capability to produce believable data at high enough altitudes to reach such a region, or the regions normally used have become populated with aerosols.

10.3 DIAL

For completeness, we introduce DIfferential Absorption Lidar (DIAL) which makes use of absorption features unique to specific atmospheric constituents. DIAL is not used for aerosol measurements. Two wavelengths are used, one on-peak, within the absorption band, and one off-peak, outside of the absorption band. Assuming no other atmospheric constituents absorb with any degree of significance in the chosen wavelengths, then differences in on- and off-peak absorption should be due to changes resulting from the species of interest. DIAL measurements, relying on absorption, are generally made of gaseous species, such as

ozone. Also, due to the nature of the atmosphere, especially the troposphere, wavelengths in the ultraviolet spectrum are most common, with the possibility for systems ranging from UV to near IR (Gimmestad, 2005).

As before, DIAL begins with Equation (10.1), the lidar equation. However, both the on- and off- peak wavelengths used have a separate lidar equation. The difference in atmospheric extinction, as stated above, is due to the gas species to be measured, and is expressed

$$\Delta\sigma_a = N\Delta C_a, \tag{10.20}$$

where

$$\Delta C_a = C_a(\lambda_{on}) - C_a(\lambda_{off}), \tag{10.21}$$

N is molecular number density of the gas species, and $C_a(\lambda)$ is the absorption cross-section at wavelength λ.

Since the lidar constant and overlap function are system-related, a ratio of the on- and off-peak lidar equation yields

$$\frac{P_{on}(R)}{P_{off}(R)} = \frac{\sigma_{b,on}(R)}{\sigma_{b,off}(R)} \exp\left[-2\int_0^R \Delta\sigma_a(r)\mathrm{d}r\right]. \tag{10.22}$$

In most cases, the difference between on- and off-peak wavelengths is on the order of a few nm, making it possible to assume that the corresponding backscatter coefficients are equal. With this assumption, solving Eq. (10.22) for $\Delta\sigma_a(R)$ and substituting Eq. (10.20) produces the number density,

$$N(R) = \frac{1}{2\Delta C_a}\left[\frac{\mathrm{d}}{\mathrm{d}R}\ln\left(\frac{P_{on}(R)}{P_{off}(R)}\right)\right]. \tag{10.23}$$

However, the assumption that the backscatter coefficient at each wavelength is constant can impose significant errors even over small differences in wavelength (Fredriksson and Hertz, 1984). Also, the lidar constant might not be equal at both wavelengths due to differences in optics or the use of multiple lasers. Furthermore, a generalization of extinction due to molecular and other aerosols in the atmosphere should be included for completeness. Extending Eq. (10.22) with these considerations yields

$$\frac{P_{on}(R)}{P_{off}(R)} = C' \frac{\sigma_{b,on}(R)}{\sigma_{b,off}(R)} \exp\left\{-2\int_0^R \left[\Delta\sigma_{a,g}(r) + \Delta\sigma_{a,a}(r) + \Delta\sigma_{a,m}(r)\right]\mathrm{d}r\right\}, \tag{10.24}$$

where $C' = C_{on}/C_{off}$ is a new lidar constant, and the subscript g represents the gaseous spe-

cies to be measured. $\Delta C_{a,a}(R)$ may further be separated into an aerosol component and a component for other known gases absorbing at those wavelengths.

Solving Eq. (10.24) for N yields

$$N(R) = \frac{1}{\Delta C_{a,g}} \left\{ \frac{1}{2} \frac{\mathrm{d}}{\mathrm{d}R} \ln \left[\frac{P_{on}(R)\sigma_{b,off}(R)}{P_{off}(R)\sigma_{b,on}(R)} \right] - \Delta C_{a,m}(R) - \Delta C_{a,a}(R) - \Delta C_{a,og}(R) \right\} \quad , \quad (10.25)$$

where the subscript "*og*" denotes absorption due to other gaseous species. As before, molecular effects may be modeled or otherwise determined through measurements. The particulate aerosol contribution can be determined in the same measurement if using a multiple wavelength lidar with a harmonic providing the DIAL wavelengths and methods presented in this chapter. The final term, due to other gases, is dependent on the wavelengths used and the gas of interest. The relative error introduced is dependent upon the strengths of the measured gas and interfering gases' absorptions. While potentially negligible, the error may be significant (Gimmestad, 2005).

As might be expected, specific laser wavelengths are more useful for different species. Ignoring common, non-aerosol uses for DIAL such as O_3, ultraviolet systems have shown capable of measuring atmospheric SO_2, Cl_2 , NO_2, and even Hg (Egeback et al., 1984; Edner et al., 1987, Edner et al., 1989). Visible systems have also been employed to measure SO_2, NO, and NO_2 (Fritzsche and Schubert, 1997; Kolsch et al., 1989), but also industrial and vehicular emissions (Swart and Bergwerff, 1990; Toriumi, Tai, and Takeuchi, 1996). More unique industrial emissions, including hydrocarbons, complex molecules, and high-temperature combustion products, are detectable in the infrared spectrum (Murray and van der Laan, 1978; Rothe, 1980; Killinger and Menyuk, 1981). However, the atmosphere is active in the infrared region. As a result, the potential for species such as water vapor, which are highly variable with strong absorption features to interfere, is large, and wavelengths must be chosen carefully. A number of studies have shown the feasibility and analyzed potential errors in infrared DIAL measurements (Menyuk and Killinger, 1983; Ambrico et al., 2000). The potential uncertainty has led to slower adoption of infrared DIAL techniques in favor of UV and visible measurements (Gimmestad, 2005).

10.4 Raman

Raman scattering presents another multiwavelength approach to lidar retrievals of aerosol parameters. Unlike DIAL or High Spectral Resolution Lidar (HSRL) approaches using two laser-generated wavelengths, Raman scattering utilizes shifts in a single wavelength due to inelastic scattering with particles. Raman scattering processes produce shifts of constant wavenumber as a photon excites the scatterer into (typically) higher rotational or vibrational states. Though wavelength shifts to shorter wavelengths are possible, under typical atmospheric conditions, shifts to longer wavelengths, or Stokes scattering, corresponding

to a decrease in photon energy are favored. Contrast this with Mie scattering theory, which assumes elastic collisions with spherical particles where no energy is lost in the collision. Raman scattering is on the order of 500–1000 times weaker than molecular scattering for the vibrational case, and is most effectively used in regimes where signal-to-noise is usually high, such as in the lower atmosphere where scattering is more likely or during the night when solar background is at a minimum. Nitrogen (N_2) is the most commonly used Raman scatterer, though oxygen (O_2) scattering is not uncommon (Whiteman et al., 1992). One of the first atmospheric applications of Raman scattering, in this case water vapor, was accomplished by Melfi et al., (1969).

Numerous ground-based Raman lidar systems are active throughout the world, such as the Department of Energy Atmospheric Radiation Measurement (ARM) Climate Research Facility (CRF) Raman lidar (CARL) (Goldsmith et al., 1998). CARL has provided a climatological database of aerosol and water vapor profiles since 1996 over the ARM Southern Great Plains (Turner et al., 2001). CARL demonstrates the viability of Raman lidar systems when compared with traditional airborne Sun photometer measurements, producing aerosol extinction profiles with systematic uncertainties of about 6% (355 nm). This is within the typical range of 15–20%, or 0.025 km^{-1}, whichever is larger, for state-of-the-art instruments (Schmid et al., 2006). Multiwavelength Raman lidar systems have been used to retrieve vertical profiles of aerosol optical and microphysical parameters such as single-scattering albedo, aerosol absorption, refractive index, and effective radius. Both simulations and field measurements have confirmed the accuracy of these retrievals by Raman lidar (Müller et al., 2001a, 2001b, 2002; Veselovskii et al., 2002; Wandinger et al., 2002).

As noted earlier, the shift in wavelength is constant in the wavenumber domain and is independent of whether the scattering is Stokes or anti-Stokes. Considering the case of nitrogen, the vibrational transition is 2330.7 cm^{-1}. A tripled Nd:YAG laser output with fundamental frequency 1064 nm would shift from 354.7 nm to 386.7 nm, while a doubled Nd:YAG laser will shift from 532 nm to 607.3 nm, assuming Stokes scattering. Since such shifts are unique for atmospheric molecular constituents, they are useful in separating aerosol from molecular scattering effects.

Consider that transmission for photons traveling from the lidar is at the wavelength transmitted from the laser, while the return signal is at the Raman-shifted wavelength. Thus, Eq. (10.1) can be written for Raman scattering as

$$P_R(R) = P_0 \frac{c\Delta t}{2} \frac{A\eta_R}{R^2} O_R(R)\sigma_{b,R}(R) \exp\left\{-\int_0^R \left[\sigma_e(r,\lambda_0) + \sigma_e(r,\lambda_R)\right] \mathrm{d}r\right\}, \tag{10.26}$$

where the subscript "*R*" is used to denote Raman components, and the subscript "0" denotes the laser wavelength components.

The backscatter coefficient for the Raman scattering may be expressed as

$$\sigma_{b,R} = N_R(R) \frac{dC_R}{d\Omega}(\pi, \lambda_0), \tag{10.27}$$

where $\frac{dC_R}{d\Omega}(\pi,\lambda_0)$ is the Raman backscatter cross section.
Substituting Eq. (10.27) into Eq. (10.26) and solving for extinction yields

$$\sigma_e(R,\lambda_0)+\sigma_e(R,\lambda_R)=\frac{\mathrm{d}}{\mathrm{d}R}\ln\left[\frac{N_R(R)}{X_R(R)}\right]+\frac{\mathrm{d}}{\mathrm{d}R}\ln\left[O(R,\lambda_R)\right]\ . \tag{10.28}$$

Separating molecular and aerosol components further provides

$$\sigma_{e,a}(R,\lambda_0)+\sigma_{e,a}(R,\lambda_R)=\frac{\mathrm{d}}{\mathrm{d}R}\ln\left[\frac{N_R(R)}{X_R(R)}\right]-\sigma_{e,m}(R,\lambda_0)-\sigma_{e,m}(R,\lambda_R)\ , \tag{10.29}$$

assuming total laser/receiver overlap. In regions close to the receiver, the overlap function can be a major source of uncertainty due to the logarithm of a rapidly decreasing function as one approaches the receiver, as well as a mismatch of the etendue of the receiver and transmitter.

To simplify future expressions, overlap will be assumed complete ($O(R) = 1$). Also note that only Raman scatterer number density is dependent upon range in the backscatter coefficient expression. For nitrogen or oxygen, number densities are typically modeled using a standard atmosphere or directly measured through means such as balloon soundings of temperature and pressure.

To further consolidate Eq. (10.29), the Ångström exponent is introduced. The Ångström exponent relates the extinction at two different wavelengths as

$$\frac{\sigma_e(R,\lambda_1)}{\sigma_e(R,\lambda_2)}=\left(\frac{\lambda_2}{\lambda_1}\right)^{\alpha(R)}\ , \tag{10.30}$$

where $\alpha(R)$ denotes the Ångström exponent at distance R from the lidar.

Substituting Eq. (10.30) into Eq. (10.29) for the transmitted aerosol extinction yields

$$\sigma_{e,a}(R,\lambda_0)=\frac{\frac{\mathrm{d}}{\mathrm{d}R}\ln\left[\frac{N_R(R)}{X_R(R)}\right]-\sigma_{e,m}(R,\lambda_0)-\sigma_{e,m}(R,\lambda_R)}{1+\left(\frac{\lambda_0}{\lambda_R}\right)^{\alpha(R)}}. \tag{10.31}$$

In cases where the difference between wavelengths is small, such as in rotational Raman scattering, the denominator can be approximated as 2.

The corresponding backscatter coefficient at the emitted wavelength can also be derived. The signals from both elastic backscatter (P) and Raman scattering (P_R) of the desired wavelength are retrieved at the desired altitude (R) and at a reference altitude (R_0)

where no aerosol is assumed to exist. This is typically a region of the upper troposphere, though care should be taken in the event of aerosol loading common from fires or volcanic events. Begin by forming the ratio (Ansmann et al., 1992),

$$\frac{P_R(R_0)P(R)}{P_R(R)P(R_0)} = \left[\frac{O_R(R_0)O(R)}{O_R(R)O(R_0)}\right]\left[\frac{\sigma_b(R_0,\lambda_R)\sigma_b(R,\lambda_0)}{\sigma_b(R,\lambda_R)\sigma_b(R_0,\lambda_0)}\right]\frac{\exp\left[-\int_{R_0}^{R}\sigma_e(r,\lambda_0)\,dr\right]}{\exp\left[-\int_{R_0}^{R}\sigma_e(r,\lambda_R)\,dr\right]}, \tag{10.32}$$

using Eq. (10.1) for the elastic signal and Eq. (10.26) for the Raman signal. Note that in the case that the overlap for both wavelengths is the same ($O=O_R$) the expression is insensitive to overlap conditions. Using this assumption, substituting Eq. (10.27) for the Raman backscatter coefficients, separating molecular and aerosol components from the elastic backscatter coefficients, and solving for backscatter at range R yields

$$\sigma_{b,a}(R,\lambda_0)+\sigma_{b,m}(R,\lambda_0) = \left[\frac{P_R(R_0)P(R)}{P_R(R)P(R_0)}\right]\left[\frac{N_R(R)}{N_R(R_0)}\right]\left[\sigma_{b,a}(R_0,\lambda_0)+\sigma_{b,m}(R_0,\lambda_0)\right] \times\frac{\exp\left[-\int_{R_0}^{R}\sigma_e(r,\lambda_R)\,\mathrm{d}r\right]}{\exp\left[-\int_{R_0}^{R}\sigma_e(r,\lambda_0)\,\mathrm{d}r\right]}. \tag{10.33}$$

Equation (10.33) can be further simplified by choosing a particle-free region of the atmosphere as the reference altitude in order to eliminate the aerosol contribution to backscatter at that altitude. The molecular contributions to backscatter may then be modeled as before. The extinction profiles at the two wavelengths can be estimated from Eq. (10.31) and the spectral dependence assumed in Eq. (10.30). Finally, the lidar ratio could be determined once extinction and backscatter are known.

The total molecular contribution to backscatter around the laser wavelength consists of an elastic component and a distribution of wavelength-shifted components that result from quantum excitations in the rotational energy of the scattering molecules (primarily O_2 and N_2). The laser-induced excitations can either enhance or reduce molecular rotational energy, producing discrete spectral lines of scattered light with higher (Stokes) or lower (anti-Stokes) wavelengths, respectively, relative to the wavelength of the laser. The distribution of scattered radiation around the central laser line depends on wavelength and temperature. The Raman cross section in Eq. (10.27) characterizing the molecular backscatter for a given rotational Raman line (λ_R) relative to the central wavelength (λ_0) is a function of not only wavelength but also temperature and thus altitude (Whiteman, 2003; Di Girolamo et al., 2004), so the computation of the backscatter coefficient in Eq. (10.33) using portions of the rotational Raman spectrum requires knowledge of both the number density and temperature profiles. However, since the intensity distribution for the pure rotational Raman spectrum near the laser excitation wavelength depends on temperature, it is possible to extract temperature information from measurements of multiple rotational Ra-

man bands. The power ratio for two Raman signals with different wavelengths (rotational quantum numbers J_1 and J_2) in the pure rotational Raman spectrum is given as a function of temperature (T) by the expression (Penney et al., 1976)

$$\frac{P_{J_2}(R)}{P_{J_1}(R)} = \exp\left[\frac{\mathrm{a}}{\mathrm{T'}\,(R)} + \mathrm{b}\right] \quad , \tag{10.34}$$

where a and b are calibration constants that can be determined from local radiosonde data. The exact functional form of Eq. (10.34) is strictly valid for single Raman lines but can also be used to approximate the relationship between signals measured through physical passband filters with nonzero spectral widths (Di Girolamo et al., 2004). Figure 10.4 shows measurements of two rotational Raman signals and one elastic scattering signal in the UV taken at night on June 24, 2009 in Hampton, Virginia. Visible in the elastic profile, but not in the molecular returns, is a cloud from about 2.4-2.9 km altitude. Figure 10.5 illustrates the temperature profile retrieved using Eq. (10.34) in comparison with a radiosonde profile.

Alternatively, given a temperature profile and suitable calibration constants, the total Raman response expected in one passband can be determined from the measured Raman signal transmitted through a filter with a different passband. Since the effective Raman backscatter crosssection corresponding to the signal measured through a practical filter must be integrated over the spectral range of the filter passband, it can be difficult to determine precisely for a real lidar system. By exploiting the relationship between portions of the rotational Raman spectrum (Eq. 10.34), the measured Raman signal can be converted to a corresponding signal from another passband for which the precise Raman cross section is known. The ratio of the elastic to Raman lidar equations, evaluated at range R, gives

$$\frac{P(R)}{P_R(R)} = \frac{C_1}{C_2}\left[\frac{O(R)}{O_R(R)}\right]\left[\frac{\sigma_b(R,\lambda_0)}{\sigma_b(R,\lambda_R)}\right]\frac{\exp\left[-\int_0^R \sigma_e(r,\lambda_0)\,\mathrm{d}r\right]}{\exp\left[-\int_0^R \sigma_e(r,\lambda_R)\,\mathrm{d}r\right]}, \tag{10.35}$$

where C_1 and C_2 are the elastic and Raman lidar constants, respectively. Assuming that the lidar system is aligned such that the overlap function is insensitive to wavelength (O=O_R) and the atmospheric transmissions at the laser and Raman-shifted wavelengths are approximately the same (so that the ratio of exponentials goes to unity), Eq. (10.35) can be rearranged to yield

$$\sigma_b(R,\lambda_0) = \frac{C_2}{C_1} \times \frac{P(R)\sigma_b(R,\lambda_R)}{P_R(R)} \quad , \text{or}$$

$$\sigma_{b,a}(R,\lambda_0)+\sigma_{b,m}(R,\lambda_0)=$$

$$\frac{C_2}{C_1}\times\frac{P(R)\sigma_b(R,\lambda_R)}{P_{J_1}(R)\exp\left[\dfrac{a}{T'(R)}+b\right]}=\frac{P(R)\sigma_b(R,\lambda_R)}{P_{J_1}(R)\exp\left[\dfrac{C_3}{T'(R)}+C_4\right]}, \tag{10.36}$$

where the last expression comes from substituting P_{J_2} in Eq. (10.34) for P_R in Eq. (10.35), which is considered to be the Raman response over a passband for which a good cross section is known. The calibration constants, C_3 and C_4, can be obtained experimentally from clear-sky (aerosol-free) measurements with small elastic (aerosol) returns such that the aerosol backscatter coefficient in Eq. (10.36) can be neglected. With two precalibrated Raman passbands for retrieving temperature according to Eq. (10.34), an elastic scattering measurement (P), number density profile, and appropriate values for the cross section and calibration constants, Eq. (10.36) can be used to obtain the backscatter coefficient. Figure 10.6 shows aerosol backscatter coefficient retrievals for the same night as in Figure 10.4 using the rotational Raman method and the Fernald elastic inversion method with assumed

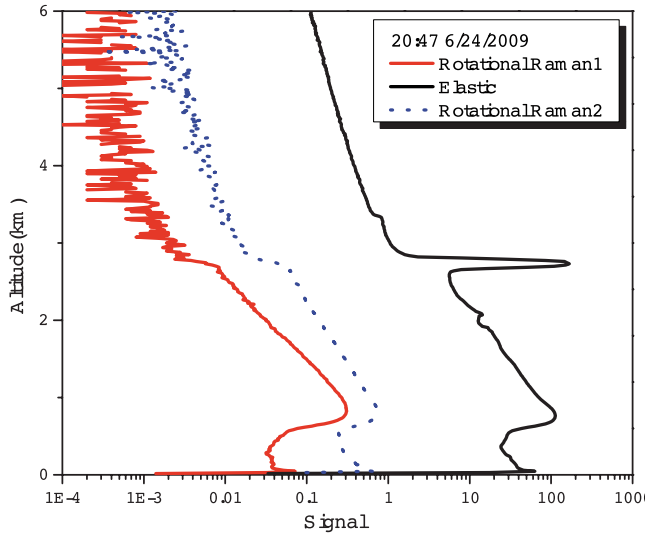

Figure 10.4 Two rotational Raman scattering profiles at 354.2 and 353.35 nm and one elastic scattering profile at 355 nm measured over Hampton University on June 24, 2009.

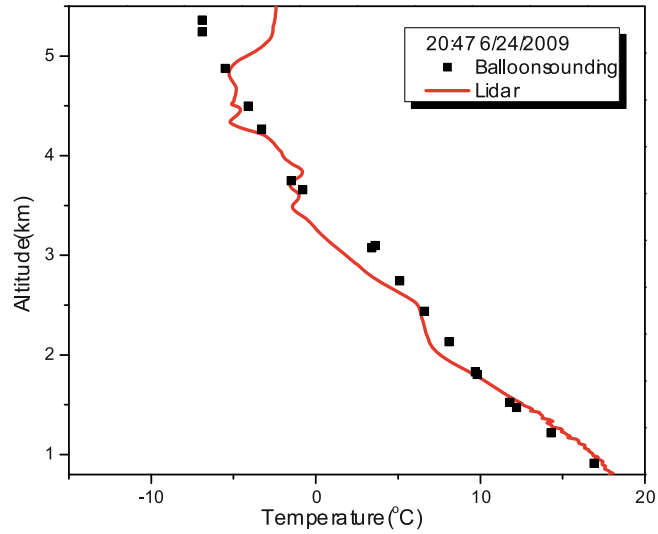

Figure 10.5 Temperature profile retrieved from Raman lidar measurements compared with a radiosonde at 20:47 (local time) over Hampton University on June 24, 2009.

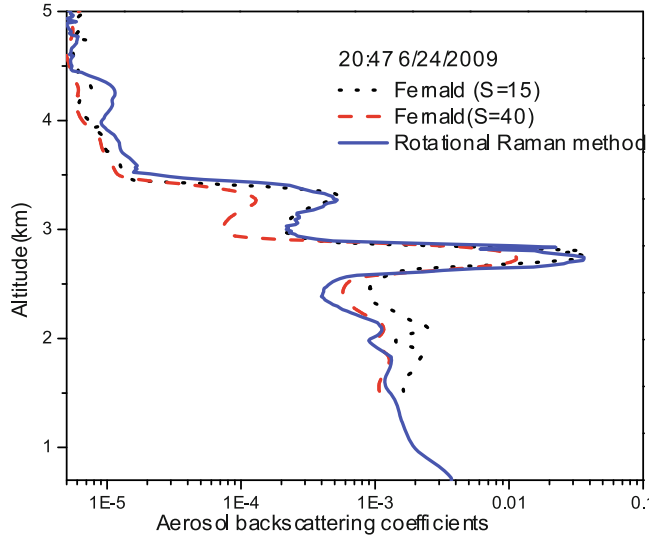

Figure 10.6 Atmospheric aerosol backscatter coefficients obtained with the rotational Raman method and the Fernald/Klett technique with assumed lidar ratios of 15 and 40 sr over Hampton University on June 24, 2009.

lidar ratios of 15 and 40 sr. The rotational Raman profile indicates that the lidar ratios above and below the cloud seen at 2.5 km altitude are different. The cloud has a lidar ratio of 15 sr, while aerosol loading increases the extinction coefficient and the lidar ratio to about 40 sr below the cloud. Additionally, reliable retrievals from the rotational Raman method extend to lower altitudes than those obtained using the Fernald method because the ratio in Eq. (10.35) greatly diminishes the effects of the overlap function at close range if the lidar detector system is aligned consistently for all wavelengths.

10.5 HSRL

As with Raman scattering presented in the previous section, High Spectral Resolution Lidar (HSRL) presents a multiwavelength approach to separating molecular and aerosol contributions to lidar retrievals. Thermal motion in particles causes Doppler broadening of the range of wavelengths accepted by the particles for scattering and absorption. Since this effect is dependent upon the particle's mass, larger aerosol particles will exhibit lower degrees of broadening than atmospheric molecular constituents. The high spectral resolution technique makes use of the differences in linewidth broadening to separate molecular Rayleigh components of scattering from Mie-regime scattering of aerosols. The derivation is precisely the same as presented in Section 10.4, where the subscript "R" would instead denote "Rayleigh" as opposed to "Raman". As a result, no derivation will be presented for the lidar equation, though the underlying physics and techniques for measuring at high spectral resolution will be discussed. The strongest difference, however, is High Spectral Resolution Lidar (HSRL) provides a means to directly measure the aerosol contribution to the signal separate from the molecular contribution.

The process by which molecules scatter light in a range outside their fundamental wavelength is known as "broadening". The three forms of broadening exhibited in the atmosphere are natural, pressure, and Doppler broadening. Natural broadening is a side-effect of Heisenberg uncertainty, where the knowledge of stored energy versus the lifetime of the excited state is constrained via the uncertainty principle. However, the effect is negligible outside of extreme atmospheric reaches where individual molecules can be considered free.

Pressure broadening is a form of dampening whereby collisions lead to de-excitations of molecular states. For pressure broadening to be significant, the mean free path between molecules must be short enough that the time between collisions is shorter than the lifetime of the excited state. Doppler broadening, by contrast, is a Doppler shift of absorbed and emitted radiation due to random, thermal motion. Though the effect is less significant than pressure broadening at low, near- Earth altitudes, the effect becomes exponentially more important with altitude.

The Lorentz profile for pressure broadening is given in terms of the spectral shape factor (Φ) by

$$\Phi_L(f) = \frac{\alpha_L}{\pi\left[(f - f_0)^2 + \alpha_L^2\right]} \quad , \tag{10.37}$$

where f is the broadened frequency of the photon, f_0 is the initial frequency, and α_L is the Lorentzian Full-Width Half-Max (FWHM). The magnitude of the broadening takes the form of a Cauchy or Lorentz distribution centered about the initial photon wavelength.

Comparatively, the Doppler profile for the absorption cross section is given by

$$C_a(f) = S\Phi_D(f) = \frac{S_L}{\alpha_D\sqrt{\pi}} \exp\left[-\frac{(f-f_0)}{\alpha_D^2}\right], \tag{10.38}$$

where S_L represents the line strength of the profile and α_D is the Doppler width defined as

$$\alpha_D = \frac{f_0 v_0}{c},$$

where v_0 is the particle's speed and c is the speed of light. Note that in this case, the shape of the profile is Gaussian with line width $\alpha_D\sqrt{\ln 2}$.

Finally, combining the two probabilistic distributions in Eqs (10.37) and (10.38) into a single profile known as the Voigt profile produces (Thomas and Stamnes, 1999)

$$C_a(f) = S\Phi_V(f) = \frac{S_a}{\pi^{3/2}\alpha_D}\int_{-\infty}^{\infty} \frac{e^{-y^2}\mathrm{d}y}{(f-y)^2 + a^2}, \tag{10.39}$$

where a is known as the damping ratio, α_L/α_D.

Since aerosols are far more massive than molecules, the degree of broadening will tend to be far lessened. Thus, an atmospheric scattering or absorption profile with aerosols present will see a sharp peak near the fundamental wavelength if the aerosol is sensitive to that wavelength, and then a broader range of accepted wavelengths due to the Rayleigh scattering molecular component. Due to the relatively small nature of the broadening effects, a high degree of measurement precision is necessary to achieve the spectral resolution to measure on- and off-peak. The aerosol contribution to broadening is also often confined within the linewidth of the laser (Eloranta, 2005). To achieve this precision, Fabry-Perot interferometers or absorption filters are used to greatly limit the accepted wavelengths and produce a retrieved spectrum.

Fiocco et al. (1971) first showed the possibility of using a scanning Fabry-Perot interferometer for HSRL measurements. Improvements to this technique using a stationary Fabry-Perot interferometer have also been demonstrated (Shipley et al., 1983; Grund and Eloranta, 1991). The molecular component is commonly predicted from model estimations, and perturbations from this curve are taken as aerosol contributions. The contributions from molecular and aerosol scattering are ratioed as in the Raman technique presented in Section 10.4. The scanning technique requires longer measurement times to produce a usable spectrum. Furthermore, narrowband filters required for the desired spectral resolution can reject too much of the molecular contribution. This requirement lowers lidar efficiency and decreases signal-to-noise.

The stationary technique alleviates much of this problem by focusing solely on the region central to the laser's frequency. Aerosol and molecular contributions are measured

simultaneously and independently, thereby lowering the amount of time necessary for accurate measurements. The tuning is also non-specific and may be used at any wavelength, though any initial setup of the etalons requires a great deal of precision to maintain the method's benefits.

Alternatively, methods using atomic and molecular absorption filters to produce the narrow wavelength bands have also been used. Initial techniques used heated vapor filters to measure atmospheric temperature, backscatter, and optical depth (Shimizu et al., 1983). Improvements simplifying this technique and reducing power requirements occurred when the atomic barium filters were replaced by molecular iodine filters (Piironen and Eloranta, 1994). It should be noted that this change, while more efficient, also corresponded to the

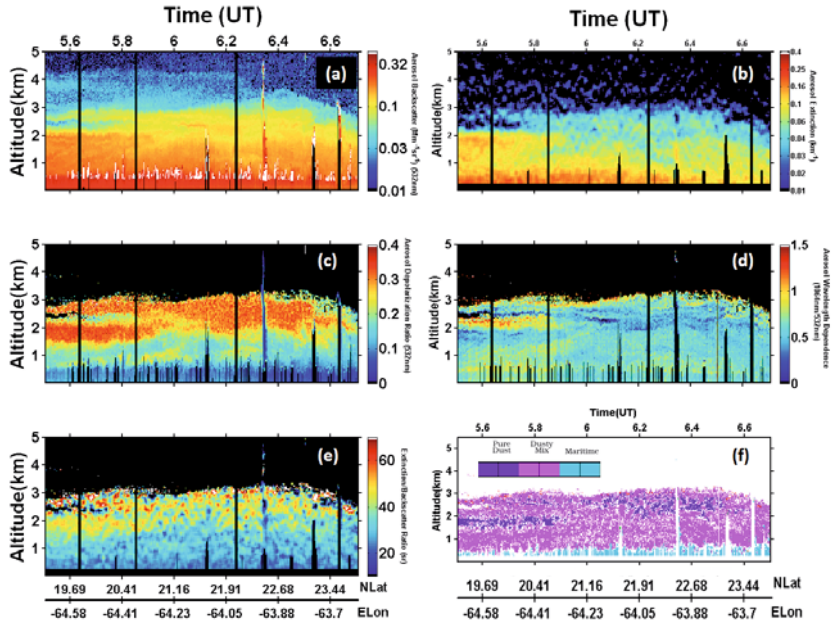

Figure 10.7 NASA Langley airborne HSRL measurements of aerosol backscatter (a), extinction (b), depolarization (c), backscatter Ångström exponent (d), and lidar ratio (e) acquired on August 24, 2010 during a flight over the Atlantic Ocean north of St. Croix, USVI. This segment covers a distance of about 430 km. The white areas below 1 km in (a) represent clouds within the marine boundary layer; these clouds attenuate the laser beams producing the small dark vertical bands below the clouds shown in these panels. The HSRL measurements of aerosol intensive parameters shown in (c–e) were used in a qualitative classification scheme to infer the aerosol type shown in (f). In this case, maritime (i.e. sea salt) aerosols are below about 600 m and Saharan dust is present between 600 m and 3 km. (Courtesy of Richard A. Ferrare).

growing availability of Nd:YAG lasers, capable of producing a 532 nm beam, to which the filters could be thermally-tuned.

Like Raman systems, ground-based and airborne HSRL systems have been used to study aerosols and clouds. Since 2005, the Arctic High Spectral Resolution Lidar (AHRSL) is one such ground-based HSRL system and is part of NOAA's SEARCH (Study of Environmental Arctic Change) contribution to the Canadian Network for the Detection of Atmospheric Change (CANDAC) facility (Eloranta, 2005, 2006). The AHSRL has measured calibrated backscatter, optical thickness, and depolarization profiles (532 nm), which are valuable for investigating aerosol properties over the Arctic (O'Neill et al., 2008; Saha et al., 2010).

NASA Langley Research Center (LaRC) (Hair et al., 2008; Obland et al., 2008) and the German Aerospace Center (DLR) (Esselborn et al., 2008) have also developed airborne HSRL systems. The LaRC HSRL has acquired over 1000 hours of data to date during more than 300 research flights since 2006, and measures backscatter color ratio ($\sigma_{b,1064}/\sigma_{b,532}$) with an additional elastic channel at 1064 nm, as well as depolarization at both 532 nm and 1064 nm. Systematic errors for derived aerosol extinction profiles are 15–20% for visible when compared with airborne sun photometer and *in situ* measurements (Rogers et al, 2009). Figure 10.7 shows an example of the suite of measurements acquired by the LaRC HSRL on August 24, 2010 during a flight segment over the Atlantic Ocean north of St. Croix, USVI. Figures 10.7a and 10.7b show aerosol extensive parameters (backscatter and extinction (532 nm), respectively) and Figures 10.7c, 10.7d, and 10.7e show aerosol intensive parameters (linear particulate depolarization (532 nm), backscatter Ångström exponent (1064/532 nm), and aerosol lidar ratio (532 nm), respectively). The white areas at altitudes between 0.5 and 1 km in Figure 10.7a correspond to small cumulus clouds in the marine boundary layer. Intensive parameters are insensitive to aerosol amount and variations in these parameters correspond to changes in the aerosol optical and microphysical properties associated with different aerosol types. In this example, a layer of Saharan dust extends from about 0.6 to 3 km above the marine boundary layer. The HSRL measurements show that the dust has higher particulate depolarization and lidar ratio than the sea salt aerosols within the marine boundary layer below 0.5 km. LaRC HSRL measurements of aerosol intensive parameters were used in a qualitative classification procedure to group the data into major significant categories (Burton et al., 2011). Eight distinct types with different aerosol intensive properties were identified. Figure 10.7f shows how this classification scheme identifes the dust and maritime aerosols in this example. The HSRL measurements have also been used to derive aerosol optical depth (AOD) and apportion AOD to these different aerosol types (Burton et al., 2011). DLR airborne HSRL measurements of aerosols including dust (Esselborn et al., 2009) have proven valuable for evaluating satellite AOD measurements (Kahn et al., 2009).

10.6 Depolarization

Previous sections have dealt with retrieval of optical properties relating to number density and composition or type of scattering or absorbing aerosols. Depolarization techniques provide a means by which the non-sphericity of scattering aerosols may be determined.

Basic Mie theory assumes spherical scatterers which do not change the state of linear polarization of light relative to the incident beam when reradiating in the backscatter direction (Bohren and Huffman, 1983). However, atmospheric aerosols commonly take shapes that may be fractal, as in the case of freshly formed soot; irregular, as in the case of desert dust; or a variety of other shapes such as needles, discs, ellipsoids, and otherwise seemingly random. These deviations from spherical shapes can serve to alter the polarization plane of backscattered light relative to the incident plane of linearly polarized light.

The depolarization ratio at range R, $d(R)$, is defined as

$$d(R) = \frac{\sigma_{b,\perp}(R)}{\sigma_{b,\parallel}(R)} \exp\left[\tau_{\parallel} - \tau_{\perp}\right], \tag{10.40}$$

where $\sigma_{b,\perp}$ is the orthogonal component of the returned backscatter coefficient, $\sigma_{b,\parallel}$ is the parallel component, and $\tau_{\perp}$ and $\tau_{\parallel}$ are the respective optical depths. Known typical values of depolarization combined with other information such as lidar ratio, extinction coefficient, and backscatter coefficient, can help to identify unknown or ambiguous aerosol layers. Time series measurements of depolarization in persistent layers can also illustrate aerosol evolution, such as the change in volcanic aerosol from initial tephra and SO_2 to more spherical liquid sulfate aerosols.

Depolarization measurements are commonly used in cloud studies to differentiate water vapor from ice. However, aerosol depolarization measurements are known to show a strong dependence upon the aerosol size parameter, $x = 2\pi r/\lambda$, where r is the particle's radius, and λ the wavelength of the incident photon (Mischchenko and Sassen, 1998). Given the wide range of sizes aerosols may take, ranging from Rayleigh scattering regime through the Mie regime and into geometric optics, the extra information on size that can be provided through depolarization measurements is invaluable. This is especially true if combined with multiple wavelength ratio techniques.

10.7 Lidar networks

Whereas the preceding sections have described lidar theory and the various methods by which one may retrieve parameters related to aerosols, such as size distribution, number density, and detection of specific molecular species, the following sections will cover technical applications regarding lidar implementation. Lidar stations tend to be limited to a single location for each measurement. While mobile lidar stations have been constructed in the beds of trucks and vans, they tend to be kept stationary, except for short periods where they are used for a local/regional measurement campaign. Airborne and satellite-carried systems, to be discussed in the following section, expand coverage to larger regional and even global scales, but each profile is still fixed to a single location at a set time. Networks of lidars, however, while comprised of individual fixed lidar stations, provide a means to

cover a large geographical area with simultaneous measurements performed with similar equipment at each station. Some of the current leading lidar networks include the European Aerosol Research Lidar Network (EARLINET), the Global Atmosphere Watch (GAW) Aerosol Lidar Observation Network (GALION), and Goddard Space Flight Center's Micropulse Lidar Network (MPLNET).

EARLINET began in 2000 with the objective of establishing "a quantitative comprehensive statistical database of the horizontal, vertical, and temporal distribution of aerosols on a continental scale, provide aerosol data with unbiased sampling, for important selected processes and air-mass history, together with a comprehensive analyses of these data" (Schneider, 2000). While the original project period only lasted until 2003, the network has continued with volunteered support from member stations. The current implementation, EARLINET-ASOS (Advanced Sustainable Observation System), continues the EARLINET project and advances its original goals to provide multi-year continental scale datasets using state-of-the-art lidar techniques (Pappalardo, 2006). An additional project, EARLINET-CALIPSO, is also ongoing since 2008 and is aimed at providing a long-term record of groundbased lidar measurements to provide a validation record for satellite missions in response to the 28 April 2006 launch of the spaceborne lidar aboard the CALIPSO satellite, which will be discussed in detail in the next section. EARLINET is currently comprised of 15 member stations spanning Europe, a map of which can be seen in Figure 10.8. While validation efforts have been on going since CALIPSO's launch, EARLINET-CALIPSO formalized the network validation program (Pappalardo et al., 2010).

Members of EARLINET follow a set of quality standards listed in the EARLINET constitution, which can be found on their website listed at the end of this chapter. Members are expected to compare their systems and data to other member stations, pursue joint research projects, and facilitate the exchange and availability of data with other member stations. All lidars operate at any of 1064 nm, 532 nm, and/or 355 nm wavelengths for elastic backscatter retrievals. Some stations also perform Raman retrievals of aerosol backscatter and extinction, and additional retrievals of depolarization and Raman water vapor and temperature. Further system capabilities may include scanning and portability. These capabilities are defined in the NetCDF files provided by each station. These data are taken at scheduled intervals as determined by the EARLINET members in order to facilitate the goal of a four-dimensional lidar data set in space and time.

A recent example of EARLINET's effectiveness was its coordination of measurements in response to the eruptions of Eyjafjallajökull beginning 14 April 2010. The eruption itself injected over 250 million cubic meters of tephra that was lofted to a height of 9 km, which the network was able to aid in quantifying and tracking. For the two weeks following the eruption, until 30 April 2010, lidar stations in EARLINET coordinated rapid-fire communication between all members in order to watch for and track the volcanic plume and its evolution (Ansmann et al., 2010; Guerrero-Rascado et al., 2010; Wiegner et al., 2012; Groß et al., 2012). The system, by providing quicklook images via website, further enabled the flow of data between centers in near real time. Updates were also provided as they became available to Volcanic Ash Advisory Centers (VAACs). These data aided in validation of models, and helped quantify the extent of the plume's travel, rate of fallout, divergence, and other physical and dynamic characteristics exceedingly important to air traffic over Europe.

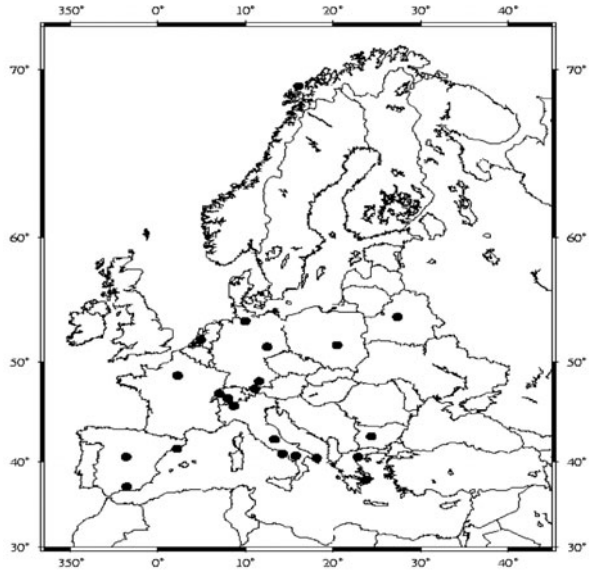

Figure 10.8 The locations of all EARLINET stations (represented by dots) as of this writing. Image produced by Pappalardo et al. (2010).

The World Meteorological Organization's (WMO) GALION network seeks to repeat the success of EARLINET on the global scale. GALION's objectives are in line with the GAW aerosol program as its goal is to determine the spatiotemporal distribution of aerosol properties related to climate forcing and air quality up to multidecadal time scales (Bösenberg et al., 2008). Data collected by GALION is intended for use in aiding the understanding of aerosol effects on climate and human health by way of air quality. These data feed climatologies, transport models and model assessments, aerosol effects on radiation, air quality forecasts, and satellite validation efforts. Though still under development, GALION members have held two workshop meetings so far, discussing measurement framework and results to date (Hoff and Pappalardo, 2010). Currently, approximately 100 lidar stations are listed to be part of GALION, with a bias toward the Northern Hemisphere in makeup due to station availability. Further information on GALION, GAW, and the WMO can be found at the WMO website and University of Maryland, Baltimore County's (UMBC) website at the end of this chapter.

NASA's MPLNET, also listed as a GALION partner, represents a specialized lidar network comprised of micropulse lidars. Micropulse lidars are made to be eye-safe and op-

erate at extremely high repetition rates using a solid state laser emitting energies on the order of microjoules at up to 10 kHz (Spinhirne, 1993, 1995). Proposed in 2000, MPLNET utilizes the advantages of smaller, more portable MPL systems in order to measure aerosol and cloud optical properties such as extinction, backscatter, and layer heights (Welton et al., 2001), as well as exploring the retrieval of multiple scattering effects in cloud layers (Berkoff and Welton, 2008). MPLNET currently consists of approximately 20 MPL stations operating on a defined analysis schedule and processing scheme (Campbell et al., 2002; Welton et al., 2010). The network has thus far been successful at measuring aerosol and cloud layers both in the PBL and lofted, polar stratospheric clouds, and their associated optical properties (Campbell et al., 2003; Campbell et al., 2008; Campbell and Shiobara, 2008; Campbell and Sassen, 2008; Campbell et al., 2008). Data are provided through the MPLNET website, provided at the end of the chapter, and are held to format standards comparable to those for satellite-based systems. Data products include raw data, backscatter signals, layer heights, profiles of extinction, backscatter, and optical depth, lidar ratio, and feature masks for clouds, aerosols, PBL height, and other relevant retrieval information.

10.8 Spacebased lidar

Lidar carries the advantages of high vertical resolution backscatter profiles, the ability to probe between clouds, and the potential to penetrate through optically thin clouds in the troposphere. While ground-stations provide useful stationary data, and aircraft provide regional data, spacecraft lidar can produce near-global data. These benefits make highly detailed spaceborne lidar retrievals down to the surface not only possible but likely.

The first airborne lidar measurements were taken from a T-33 aircraft from NASA Langley Research Center (LaRC). Simultaneous operation of a ground-based lidar provided validation measurements of the horizontal-looking system (Lawrence et al., 1968). While the original intention of this mission was detection of clear air turbulence, the development of lidar brought aerosol applications to airborne measurements as well. A year later, downward-looking lidar measurements of aerosols were made from aircraft as part of the Barbados Oceanographic and Meteorological Experiment (Uthe and Johnson, 1971).

LaRC later produced the first upward looking aircraft lidar as well as part of the validation effort for the Stratospheric Aerosol Measurement-II (SAM-II) in 1978 (McCormick, 1979). As a precursor to orbital measurements, high-altitude aircraft were flown with lidars onboard. Carried aboard the WB-57 and developed by NASA Goddard Space Flight Center (GSFC), the flight allowed for autonomous control of the aircraft and provided information about high-altitude, automated measurements necessary for spaceborne lidar retrievals (Spinhirne et al., 1982). The combination of airborne measurements provided the basis for global retrievals of aerosol constituents such as desert dust from the Sahara; Polar Stratospheric Clouds (PSCs); and stratospheric aerosols, such as from volcanic eruptions.

All of this previous work set the stage for spaceborne lidars: the LIDAR In-space Technology Experiment (LITE), L'atmosphere par Lidar Sur Saliout (The Atmosphere by Lidar on Saliout) (ALISSA), Geoscience Laser Altimeter System (GLAS), and Cloud-Aerosol

LIDAR and Pathfinding Satellite Observation (CALIPSO) instruments. LITE acted as the proof of concept mission, flying aboard Space Shuttle Discovery flight STS-64. Launched September 9, 1994, LITE employed three wavelengths using a Nd-YAG laser operating at 1064, 532, and 355 nm. Also, a boresighted camera was attached to the instrument in order to colocate actual imagery of the scenes to provide context to the lidar measurements. Additional research objectives included measurements of clouds and aerosols in the stratosphere and troposphere, PBL height, and temperature and density profiling of the stratosphere (McCormick et al., 1993). Operating for ten days, LITE provided information on the size variability, distribution, and range extent of cloud and aerosol particles in the atmosphere, and its data were used extensively in developing long-duration spaceborne lidar. Some of the novel applications include its use for determining surface wind speeds from sea surface directional reflectance measurements (Menzies et al., 1998), and its use in characterizing a super typhoon (Kovacs and McCormick, 2003).

Two years following LITE, the French-Russian endeavor ALISSA was launched on the PRIRODA module destined for MIR. Launched April 26, 1996, ALISSA utilized four Nd-YAG lasers operating at 532 nm, with objectives of determining vertical structure of clouds with absolute measurement of cloud top altitude (Chanin, 1999). A key feature is the use of four lidars operating one at a time in order to guarantee data continuity. Difficulties with MIR eventually caused interruptions in the data and the eventual end of the mission when the space station was brought back to Earth in 1999. GLAS was the first long-duration spaceborne lidar. Launched January 13, 2003, GLAS operated at 532 and 1064 nm with the main objective of using laser altimetry to measure ice-sheet topography, changes thereof, and other associated cloud and atmospheric properties (Spinhirne and Palm, 1996). Aerosol measurements were taken predominantly using the 532 nm channel. The number of observations it was able to make each year was greatly reduced (measurements were taken for approximately one to two months per year) due to a laser diode pump problem. GLAS ended its science mission in February 2010 with the failure of the last of its three lasers.

Most recently, CALIPSO was launched April 28, 2006 as a joint French-US endeavor between LaRC, France's CNES, and Hampton University. CALIPSO was placed in the Afternoon Train (A- Train) satellite constellation along with CloudSat, in order to perform simultaneous measurements of aerosol and cloud properties such as both total and layer optical depth, chemical species concentrations, polarization, and cloud properties (Goddard Space Flight Center, 2003). This information is crucial to understanding aerosol direct and indirect effects on Earth's albedo for the effects of climate change, and for determining the types, states, and development of aerosol and cloud layers. CALIPSO utilizes two Nd-YAG lasers for redundancy as part of the the Cloud-Aerosol Lidar with Orthogonal Polarization (CALIOP) instrument. Also on board are the the Infrared Imaging Radiometer (IIR) and a Wide Field Camera (WFC). All instruments operate continuously, with the exception of WFC which requires daylight to image. In addition to continuous lidar measurements, CALIOP also offers polarization measurements at 532 nm, providing both perpendicular and parallel detector channels. This distinction allows for differentiation between ice cloud and spherical aerosol particles.

As with LITE, IIR and WFC provide context to measurements taken by CALIOP. Figure 10.9 shows a typical CALIPSO curtain profile along its orbital track. The most striking feature is the distinction in the plume of Saharan dust on the right-hand side of the image.

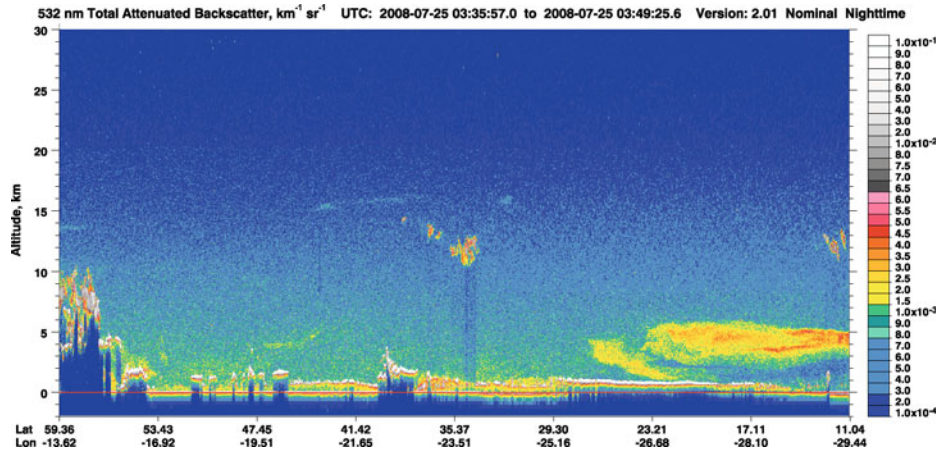

Figure 10.9 CALIPSO curtain plot taken July 25, 2008 showing an aerosol plume traveling from the Sahara. Cloud and stratospheric features are also visible.

Comparatively with the clouds shown both at high and low altitudes, particularly in the 35° latitude region, and the stratospheric features above, the aerosols are clearly visible and information about the extent of transport at profile time is provided by the plume's edge. As of this writing, CALIPSO has fired billions of shots, and only after nearly three years of near-continuous operation switched to the second laser in March 2009. CALIPSO still operates well within expected performance criteria and is expected to provide a long record of cloud and aerosol lidar measurements from space.

The CALIOP lidar on CALIPSO measures total attenuated elastic backscatter at 532- and 1064-nm wavelengths in addition to depolarization in the 532-nm channel. Since CALIOP is not a Raman lidar, an assumed value for the extinction-to-backscatter (lidar) ratio is required to derive the aerosol extinction coefficients (Liu et al., 2005). In order to obtain values of the lidar ratio for the various surface and atmospheric conditions encountered by the CALIPSO spacecraft as it orbits the Earth, the retrieval algorithm attempts to classify observed atmospheric regions with enhanced backscatter according to general aerosol type. It is assumed that the aerosol category assigned to each region consists of a mixture of particles with certain properties typically found in mesoscale air masses rather than pure aerosol systems that mix externally. The content of an aerosol mixture is determined by regional sources, wind patterns, hydration state, and chemical processes. A decision tree (Liu et al., 2005, page 48) is used to select the appropriate aerosol category assigned to a feature in a given measurement based on the mean attenuated backscatter coefficient, depolarization ratio, altitude, location, and surface type below the feature. A tabulated set of parameters corresponding to the aerosol properties of the mixture is used to compute the lidar ratio for the observed feature from Mie theory.

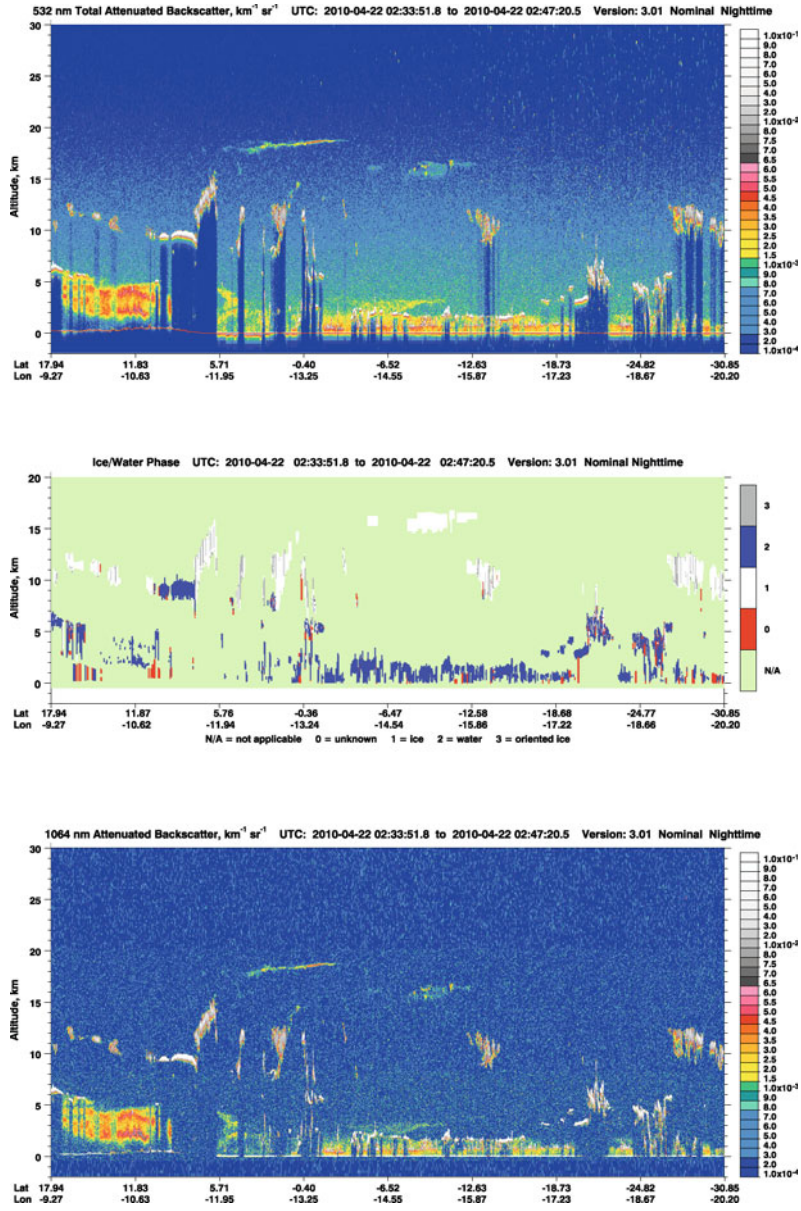

Figure 10.10 The basic measurements of CALIOP, including the total (top panel) and perpendicular (second panel) attenuated backscatter coefficients ($km^{-1}sr^{-1}$) at 532 nm as well as the total attenuated backscatter coefficient ($km^{-1}sr^{-1}$) at 1064 nm (bottom panel), are shown for a nighttime section of CALIPSO's orbit over parts of western Africa and the southern Atlantic Ocean on April 22, 2010.

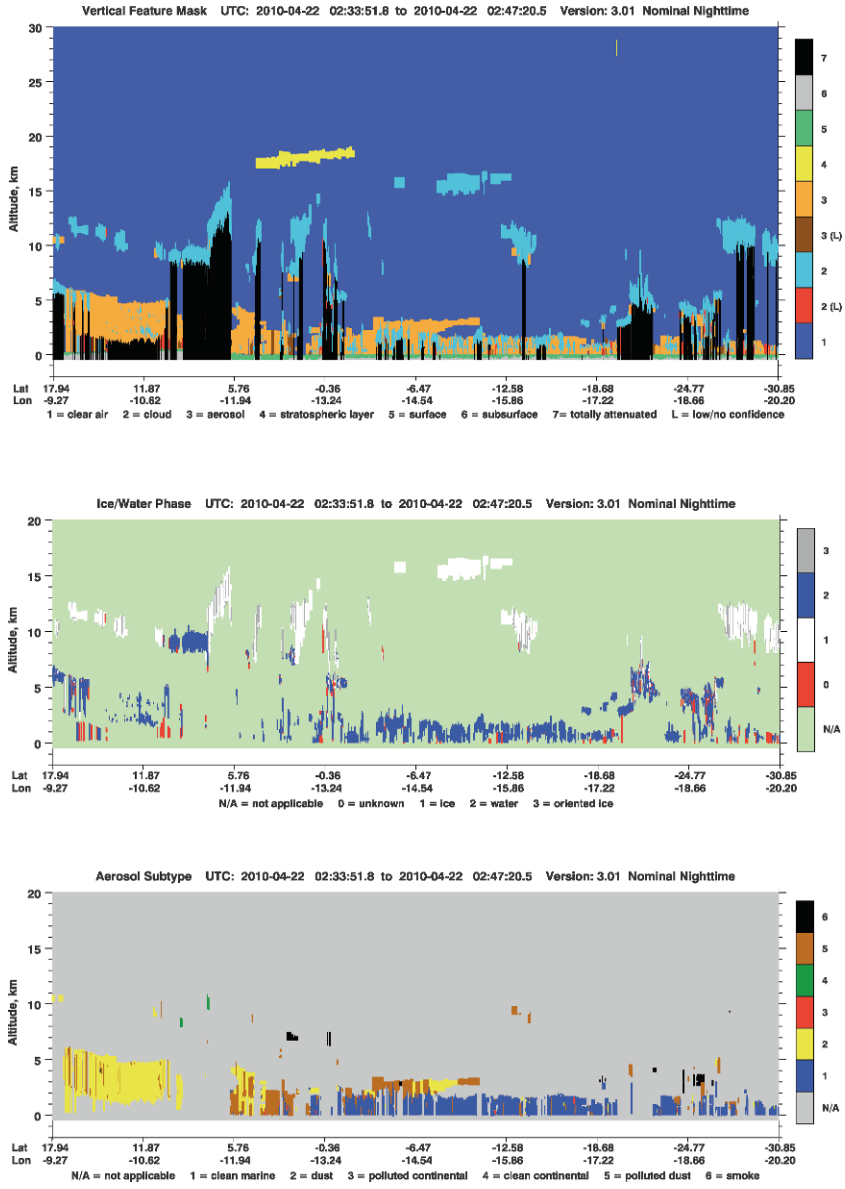

Figure 10.11 The classification of high-backscatter features into aerosol and cloud types according to CALIOP's scene classification algorithm for the same section of CALIPSO's orbit as shown in Figure 10.8. The vertical feature mask (top panel) discriminates clouds and aerosols, which are then subclassified according to cloud ice/water phase (second panel) and aerosol type (bottom panel).

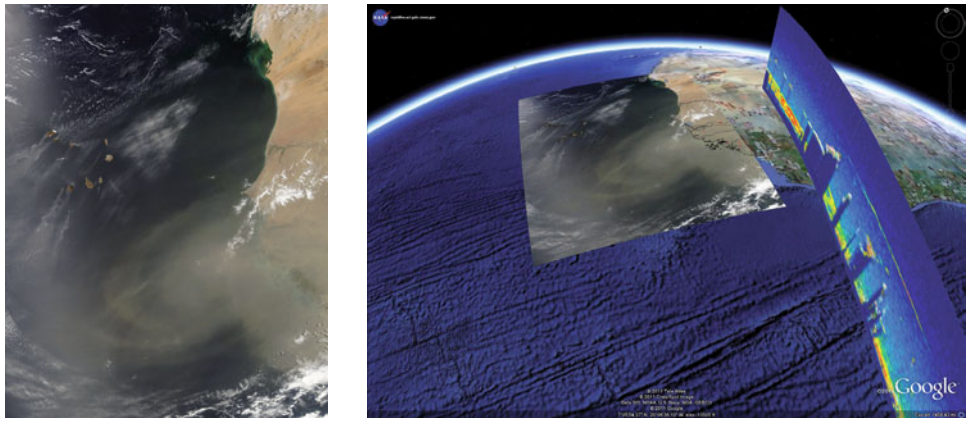

Figure 10.12 An image (left) taken by the Moderate Resolution Imaging Spectroradiometer (MODIS) instrument on NASA's Aqua satellite near the west coast of Africa on April 22, 2010, showing Saharan dust plumes being transported westward along the trade winds beneath high convective tropical clouds, and the composite (right) of this image with the CALIOP 532-nm backscatter curtain image (vertical scale exaggerated) using Google Earth.

The aerosol types and their associated optical and physical properties, which are used in the CALIOP retrieval algorithm, were identified by a clustering analysis of measured parameters obtained from AERONET, a global network of multi-wavelength sun photometers, and other sources (Liu et al., 2005). The six aerosol categories most commonly observed by AERONET are labeled as background or clean continental (containing small amounts of sulfates [SO_4], nitrates [NO_3], ammonium [NH_4], and organic carbon), marine or sea salt [NaCl], smoke (containing soot and organic carbon from biomass burning), desert dust or mineral soil, polluted dust (mixture of desert dust and smoke), and polluted continental (containing urban pollution).

Figures 10.10 and 10.11 show the basic data measured by CALIOP and the results of cloud particle and aerosol classification for a section of CALIPSO's orbit over western Africa and the Atlantic Ocean on April 22, 2010. Total attenuated backscatter ($km^{-1}sr^{-1}$) at 532 nm is shown in the first panel of Figure 10.10. The second panel shows the component of the total backscatter at 532 nm that is oriented perpendicular to the polarization of the transmitted laser pulse. Information from these two measurements yields the depolarization ratio, a quantity that indicates aerosol and cloud particle shape and thermodynamic phase. The last panel shows total attenuated backscatter profiles from CALIOP's 1064-nm channel. The color ratio between the 1064- and 532-nm channels provides information on particle size distribution.

Figure 10.11 illustrates the results of the cloud and aerosol classification algorithm for high backscatter features observed in this scene. The vertical feature mask (first panel) dis-

criminates clouds and aerosols and identifies basic features such as surface returns and total attenuation of the lidar signal below optically thick clouds. The second panel illustrates the phase (water/ice) of the water content in the clouds identified in the vertical feature mask. The third panel shows the subdivision of aerosols identified in the vertical feature mask. Evident in the figure extending southward from Africa into the Atlantic Ocean (to about 10°S latitude) near the surface to about 5 km altitude is a thick aerosol layer whose composition was identified primarily as (partially polluted) dust. Saharan dust plumes form over western Africa by convection of the hot, dry desert air and transport mineral dust westward across the Atlantic Ocean along the trade winds towards the Caribbean. It is thought that sea surface cooling from Saharan dust interferes with hurricane development in the Atlantic Ocean. The polluted content appears mostly over the Atlantic Ocean west of southern Africa. Below the dust layer south of the equator is a layer identified as clean marine (sea salt) near the surface. Also evident in the figure are high tropical convective clouds (mostly ice) and a stratospheric feature near the equator at about 18 km altitude (probably a thin cirrus cloud).

The image shown on the left in Figure 10.12 was taken on April 22, 2010 off the western coast of Africa by the Moderate Resolution Imaging Spectroradiometer (MODIS) on NASA's Aqua satellite, which orbits ahead of CALIPSO in the A-Train constellation. Low-level Saharan dust (brown) can be seen traveling westward from Africa into the Atlantic Ocean below high-altitude convective clouds (white). The image on the right is a composite of the image obtained by MODIS and the total attenuated backscatter measurements obtained from CALIOP's 532-nm channel overlaid on a picture of the Earth. The composite image was assembled using Google Earth.

10.9 Summary

Lidar instruments are important tools for studying atmospheric aerosols and cloud systems and their role in global climate, and offer several advantages over passive techniques for atmospheric remote sensing. Because they are active remote-sensing devices, employing their own light sources, lidars can make range-resolved observations along their line of sight by measuring the transit time of their laser pulses. For zenith- and nadir-looking systems this yields information on the vertical structure of the atmosphere, which is lacking in pictures and column-integrating passive sensors. Lidars are capable of making both daytime and nighttime observations of multi-layer aerosol and cloud systems with high vertical resolution. Raman and HSRL multi-wavelength observations can be used to retrieve both backscatter and extinction coefficients and to derive concentrations of atmospheric aerosols and gaseous chemical species such as carbon dioxide and water vapor, all of which are important components for understanding radiative forcing effects and global climate. Polarization-sensitive lidars can be exploited to distinguish aerosol types such as ash plumes from volcanic eruptions, biomass burning, pollution, sea salt, and dust. Depolarization from clouds gives an indication of their microphysical composition and thermodynamic phase based on cloud particle shape, allowing for the distinction of water and

ice clouds as well as nitric acid polar stratospheric clouds, which is important for understanding cloud impact on both the atmospheric radiative budget and high-latitude ozone depletion. With the advent of space-based platforms, lidars are now capable of examining the vertical structure of the atmosphere on a global scale and, unlike many passive satellite instruments including occultation devices, can penetrate down into the lower troposphere to probe the planetary boundary layer, characterizing the particulate composition of the lower atmosphere and providing a detailed picture of the atmospheric components that affect the Earth's weather and climate.

Data Website References

http://earthobservatory.nasa.gov/NaturalHazards/view.php?id=43852 (MODIS image)

http://rapidfire.sci.gsfc.nasa.gov/ (NASA/GSFC, MODIS Rapid Response, MODIS image)

http://modis.gsfc.nasa.gov/ (MODIS site)

http://www-calipso.larc.nasa.gov (CALIPSO site)

http://www.arm.gov/ (Department of Energy Atmospheric Radiation Measurement (ARM) Climate Research Facility (CRF) site)

http://mplnet.gsfc.nasa.gov/ (Micropulse Lidar Network (MPLNET) site)

http://www.earlinet.org/ (European Aerosol Research Lidar Network (EARLINET) site)

http://www.meteo.physik.uni-muenchen.de/~stlidar/quicklooks/European-quicklooks.html (EARLINET Quicklook Images site)

http://www.wmo.int (World Meteorological Organization site)

http://alg.umbc.edu/galion/ (GAW Aerosol Lidar Observation Network (GALION) site)

Acknowledgments

The authors wish to thank Michael T. Hill and Jia Su from Hampton University, for their contributions of data graphics for this chapter. In addition, the authors wish to thank Richard A. Ferrare of the NASA Langley Research Center for his contributions on Raman and HSRL field campaigns and HSRL data graphics.